*Article*

Production and Characterization of Graphene Oxide for Adsorption Analysis of the Emerging Pollutant Butylparaben

Lorena Maihury Santos Tsubouchi [1], Edson Araujo de Almeida [2], Diego Espirito Santo [3], Evandro Bona [4], Gustavo Leite Dias Pereira [5], Veeriah Jegatheesan [5], Lucio Cardozo-Filho [6], Ana Paula Peron [4,7,8] and Osvaldo Valarini Junior [4,7,*]

[1] Academic Department of Food and Chemical Engineering (DAAEQ), Federal Technological University of Paraná, Campo Mourão 87301-899, Brazil; lorenatsubouchi@alunos.utfpr.edu.br
[2] Graduate Program in Chemistry, State University of Maringá, Maringá 87020-900, Brazil; edsonalmeida2009@gmail.com
[3] Graduate Program in Environmental Engineering (PPGEA), Federal Technological University of Paraná, Francisco Beltrão 85602-863, Brazil; dsanto@alunos.utfpr.edu.br
[4] Postgraduate Program in Food Technology (PPGTA), Federal Technological University of Paraná, Campo Mourão 87301-899, Brazil; ebona@utfpr.edu.br (E.B.); anaperon@utfpr.edu.br (A.P.P.)
[5] School of Engineering and Water: Effective Technologies and Tools (WETT) Research Centre, RMIT University, Melbourne, VIC 3000, Australia; s4027614@student.rmit.edu.au (G.L.D.P.); jega.jegatheesan@rmit.edu.au (V.J.)
[6] Department of Chemical Engineering, State University of Maringa, Maringa 87020-900, Brazil; lcfilho@uem.br
[7] Postgraduate Program in Technological Innovations, Federal Technological University of Paraná, Campo Mourão 87301-899, Brazil
[8] Postgraduate Program in Environmental Engineering, Federal Technological University of Paraná, Francisco Beltrão 85602-863, Brazil
* Correspondence: osvaldovalarini@utfpr.edu.br; Tel.: +55-44-3518-1430

Abstract: Emerging pollutants such as butylparaben (BP) are often difficult to remove via conventional wastewater treatment. Therefore, this study aimed to produce and characterize graphene oxide (GO) and evaluate the adsorption of BP on this adsorbent. The GO was made using the Hummers method and characterized by TGA/DTA, XRD, XRF, BET, point of zero charge (pHpzc), SEM, and the Boehman method. Adsorption experiments were performed in a batch system. The removal efficiency from a Box–Behnken experimental design was 84.3% at a BP concentration 600 $\mu g \cdot L^{-1}$, adsorbent five $g \cdot L^{-1}$, and pH 7 in solution. The first-order (PFO) kinetics obtained the best fit to the experimental data compared to the other models tested in this study: pseudo-second-order (PSO), Elovich (ELC), and intra-particle diffusion (IPD). The Langmuir isotherm provided the best fit compared to the Freundlich isotherm. The temperature effect showed that the system has a spontaneous adsorption process, with a Gibbs energy lower than zero, and that increasing the temperature increases the adsorption capacity. The ionic effect showed that increasing the salt concentration of 1 M increased the repulsive forces but did not decrease the adsorption capacity. The regeneration cycle showed a rate of 85% up to the second cycle. The toxicity analysis confirmed the efficiency of the adsorption process using GO before and after BP adsorption on GO.

Keywords: paraben; thermodynamic analysis; physicochemical characterization; graphene; equilibrium isotherms

1. Introduction

Butylparaben (BP) (4-hydroxybenzoic acid ester) is widely found in pharmaceuticals, personal care products, and processed foods due to its chemical stability and broad-spectrum antibacterial properties [1]. Anthropogenic activities recurrently contaminate different matrices with this compound, such as water resources, sludge, sediment, soil, and drinking water [2].

BP, to date, has become an emerging pollutant in contact with the liquid medium. BP does not yet have environmental legislation, and conventional treatments do not entirely remove it from wastewater [3]. Water contamination by this paraben is the most widespread and is in the range of $\mu g \cdot L^{-1}$ in freshwater resources [1,2,4,5]. This compound is degraded relatively quickly in soil and water (on average 10 days) but is considered pseudo-persistent since it is frequently released into the environment [1].

Adverse effects assessments showed that BP, at concentrations in the $\mu g \cdot L^{-1}$ range, caused neurotransmitter dysregulation, nephrotoxicity, and cranial malformation in fish [1,6,7], infertility in male rats and in humans [4,8], and may be a potentiator in the development of breast cancer in women [6].

Methods that use advanced oxidative processes, such as ion exchange, membrane separation, heterogeneous photocatalysis, and electron precipitation, are efficient in the removal/degradation of emerging pollutants. However, these methods do not entirely remove emerging pollutants [7]. In addition, these methods generate a high amount of sludge, as well as a high demand for reagents and membrane fouling. Therefore, some of the best alternatives for removing pollutants include the adsorption process, which can use cheap, abundant materials susceptible to modification [3]. The use of adsorption methods for contamination has been gaining much prominence, as it is a very efficient method for this type of situation and has practical applications in both industry and environmental protection [8]. The method is viable because of its high removal efficiency, low operating costs, and the possibility of reusing materials considered waste in the industry [9].

The materials with the most significant potential for use in adsorption processes are those rich in carbon compounds [10]. One of their advantages is that they can be produced on a large scale. Activated carbons are porous carbon compounds that have a microcrystalline structure. Their activation receives a specific treatment that serves to increase their internal porosity since tunnels are formed inside it, which bifurcate into tunnels with an increasingly smaller diameter, creating areas of micropores; this gives the coal a gigantic internal surface and also provides good selectivity in adsorption [7].

The disadvantage of activated carbon is its high energy demand to produce the functional material. Hence, graphene oxide (GO) stands out as a material with a good capacity for adsorption and replacement of activated carbon adsorbents. GO is the oxidized form of graphene with oxygen functional groups on its surface. GO and its variations are generally prepared without exceeding the upper temperature of 250 °C; the preparation of GO from other studies is established by primary synthesis methods, which include microwave solvothermal and microemulsion methods used as efficient adsorbents for analysis of adsorption efficiency [11]. These studies used a high quantity of chemical compounds, a proposal contrary to this study that used the Hummels method, reducing the amount of chemical solvents [12–14]. These materials are non-toxic and biocompatible. In its variations, GO offers an ideal platform for adsorbing pollutants and investigating the potential of this new material. GOs have received much attention and play an essential role in separation and purification technology due to their unique properties, such as high surface area, two-dimensional structure, low weight, surface modification ability, excellent conductivity, cost-effective synthesis, and biological compatibility [15]. A growing number of studies are attempting to use the advantages that graphene composites and their derivatives offer for the sorption of a wide range of elements, including heavy metals, organic molecules, drugs, and gases [16].

There are some studies involving the adsorption process of BP. Wei et al. (2022) [17] investigated the adsorption and degradation of parabens (BP, propylparaben, ethylparaben, methylparaben) using three types of nanomaterials from the graphene family, reduced graphene oxide, multilayer graphene, and graphene oxide. In this study, hydrogen peroxide was used to aid further catalytic degradation. The study showed a low removal efficiency of parabens in GO, close to 20% at pH 6, with an adsorbent concentration of $400 \text{ mg} \cdot L^{-1}$ and pollutant of $40 \text{ mg} \cdot L^{-1}$. Moreno-Marenco et al. (2020) [18] analyzed the adsorption of BP on activated carbon from African palm shells (*Elaeis guineensis*) by

chemical modification with solutions of calcium chloride and magnesium chloride at different concentrations. The adsorbent obtained a neutral charge point of 9.13 for the best condition of activated carbon, with a more fundamental character than the others by the Boehman method. The adsorption capacity was 1.3 mmol per gram at pH 7.34, which resulted in 252.2 mg·g^{-1}. A thermodynamic study was carried out, and negative immersion enthalpy was found, indicating the exothermic nature of the adsorption process, which involves adsorbate–adsorbent and solvent–adsorbent interactions. In contrast, the adsorbate–adsorbent interaction is an endothermic process that requires energy.

Correa-Navarro et al. (2024) [3] synthesized benzoic and magnetic cellulose to remove methylparaben and BP in water and characterized the adsorbents. In addition, PFO, PSO, ELC, Weber, Morris, and Boyd models were used to investigate adsorption kinetics, and Freundlich, Langmuir, and Sips adsorption isotherms were investigated. The maximum adsorption capacity of BP for magnetic cellulose was 12.03 mg·g^{-1}. Atheba et al. (2018) [19] used low-cost activated carbon based on coconut biochar for BP adsorption. The adsorbent was characterized using BET, Boehm analysis, and studies of adsorption equilibrium, kinetics, and adsorption thermodynamics. The experimental results revealed a BP removal efficiency of over 97% at pH 7. The Langmuir, Freundlich, and Temkin isotherm models fitted the equilibrium data with a correlation coefficient greater than 0.9. The PSO kinetic model was observed to fit the adsorption data well. Thermodynamic analysis shows positive standard Gibbs free energy values. The changes were found to be endothermic with increasing randomness.

Given the facts presented, using GO for BP adsorption introduces new parameters to the adsorptive process of emerging pollutant and adsorbent systems. This configuration is of great economic interest since health and environmental problems are associated with the uncontrolled use of these emerging pollutants. To date, this is the only work that uses a GO-based compound to remove BP using a batch system without the presence of additives in the adsorption process. Therefore, this study aimed to evaluate and characterize the GO adsorbent's production and use this functional material to adsorb BP, evaluating the removal, kinetics, adsorption isotherm, ionic effect, temperature effect, and reuse of GO. To confirm the efficiency of the evaluated adsorbent, the toxicity analysis of the BP solution was conducted before and after adsorption in a biological model widely used in environmental impact studies.

2. Materials and Methods

2.1. Materials

BP (butyl 4-hydroxybenzoate, CAS 94-26-8) was purchased by Sigma-Aldrich, USA-San Louis, MO, USA. All reagents used in this study are of analytical grade. The powdered graphite, sulfuric acid (H_2SO_4), potassium permanganate ($KMnO_4$), hydrogen peroxide (H_2O_2), hydrochloric acid (HCl), of analytical grade, used to obtain the GO was purchased from Dinâmica (São Paulo, Brazil). Tween 80, sodium hydroxide (NaOH), sodium bicarbonate ($NaHCO_3$), sodium carbonate (Na_2CO_3), and sodium chloride (NaCl) were purchased in analytical grade from Synth Diadema (São Paulo, Brazil).

2.2. Graphene Oxide Production and Characterization

GO was prepared by oxidizing pure graphite; 1.0 g of the material was added to 25 mL of H_2SO_4 in a beaker. The material was then stirred constantly until it was utterly homogenized. Subsequently, 3.0 g of $KMnO_4$ was gradually added under a water bath at a temperature close to 20 °C for 20 min. We then increased the temperature to 35 °C for 180 min and placed the beaker in an ultrasonic bath with 60 min of stirring. After this, 46 mL of distilled water was added slowly under stirring, then a further 150 mL of distilled water and 10 mL of 30% H_2O_2 were added to complete the graphite reaction on GO. The product was washed with 50 mL of 5% HCl solution and then five more times with distilled water [12–14]. The centrifugation occurred at 4000 rpm, and then the GO was dried to obtain solid material.

The GO obtained was analyzed by thermogravimetric means (TGA/DTA), and approximately 2 mg of GO was weighed and placed in an aluminum holder, according to the parameters of B. C. da S. Rocha et al. (2024) [3]. The temperature profile was obtained using an Instruments thermal analyzer, model SDT Q600 (TA Instruments, New Castle, DE, USA).

X-ray diffraction (XRD) used a Bruker, Billerica, MA, USA model D2 Phaser. The samples were inserted into the equipment and received Cu, Kα radiation of 40 kV and 35 mA. The sample was analyzed at a 2θ angle between 10 and 60° with a step of 0.02° and a scanning speed of 0.58° per minute.

The BET method (Brunauer, Emmett and Teller) analyzed the adsorption–desorption isotherms of nitrogen (-196 °C) at a relative pressure range of 10^{-6} to 1 that were treated by the flow of N_2 at 250 °C. The micropores, mesopores, average diameter, and pore distribution were found using the BET method.

The GO was also characterized by the X-ray fluorescence (XRF) brand Bruker S8, model Tiger 4 kW (Bruker, USA). To run the equipment, a boric acid tablet (H_3BO_3) was prepared as an inert agent, 1 g of GO was weighed and mixed with 20 g of H_3BO_3, the mixture was homogenized, and around 7 g was removed to press and form the tablet, after which the tablet was pressed.

The zero charge point (pHpzc) was determined by evaluating the GO between pHs 1 and 12. The pH values were found by mixing 50 mg of GO with 20 mL of a mixture of NaOH and HCl solutions at a concentration of 0.1 M. Subsequently, at 25 °C, 50 rpm, for 24 h on a Tecnal TE-4200 shaker Piracicaba (Sao Paulo, Brazil), the samples were filtered, and the final pH was measured [7,20].

The functional groups of GO were evaluated using the Boehm method [7,21]. The mass concentration of 50% determined the acid groups of GO in the solvents 0.1 N NaOH, sodium bicarbonate (NaHCO$_3$), and sodium carbonate (Na$_2$CO$_3$) in separate beakers. The samples were stirred for 24 h at a temperature of 25 °C. After this period, the samples were filtered, and 10 mL was removed. Then, 10 mL of 0.1 N HCl was added to the NaOH samples, 15 mL of HCl was added to the NaHCO$_3$ samples, and 20 mL of acid was added to the Na$_2$CO$_3$ samples. The solutions were then heated, cooled, and titrated with 0.1 M NaOH with a phenolphthalein indicator. The same tests were carried out on the blank samples (without GO). The functional groups were calculated using Equation (1).

$$m_{eq} = V_t \times \frac{N_b \times (V_{am} - V_b)}{V_{al}} \times \frac{1}{m_{coal}} \tag{1}$$

where m_{eq} is the amount of basic, carboxylic, lactones, and phenolic groups (mmol·g^{-1}); carbon is defined as the mass of GO, V_t total volume, N_b is the initial concentration of NaOH, $V_{am} - V_b$ is the difference in the volumes of NaOH used to titrate the samples and the blank (mL), and V_{al} is the volume of the aliquot (mL).

Morphological analysis of the GO was carried out using scanning electron microscopy (SEM), model EVO MA 15, (Zeiss, Jena, Germany). The samples were sputter-coated with gold-palladium under an argon atmosphere not to make them electrically conductive.

2.3. Adsorption

The removal efficiency (*ER%*) was evaluated using a Box–Behnken experimental design (Table 1).

The planning and optimization was carried out in the Matlab R203a application GAMMA-GUI [22]. The variables tested in the form of factors were pollutant concentration (x_1), adsorbent concentration (x_2), and pH (x_3). The factorial design included 15 experiments, with 12 experiments varying the factors and triplicate experiments of the central point, shown in Table 1. Polynomial Equations relating the dependent and independent variables were generated, and the *ER%* process was optimized. The analysis of variance adopted in this study was 5% [10,23–25]. The experiments used the Box–Behnken design [26,27]. The variables analyzed were pollutant concentration (x_1), which varied from 0

to 600 µg·L^{-1} [28]; adsorbent concentration (x_2), which varied from 5 to 15 g [12]; and pH (x_3), ranging from 2 to 12.

Table 1. Experimental planning of the adsorption.

Run	Concentration of the Pollution (µg·L^{-1})	Adsorbent Concentration (g·L^{-1})	pH	ER%
R1	0 (−1)	5 (−1)	7 (0)	0.0
R2	0 (−1)	15 (1)	7 (0)	0.0
R3	600 (1)	5 (−1)	7 (0)	84.9
R4	600 (1)	15 (1)	7 (0)	55.9
R5	0 (−1)	10 (0)	2 (−1)	0.0
R6	0 (−1)	10 (0)	12 (1)	0.0
R7	600 (1)	10 (0)	2 (−1)	56.4
R8	600 (1)	10 (0)	12 (1)	22.3
R9	300 (0)	5 (−1)	2 (−1)	35.5
R10	300 (0)	5 (−1)	12 (1)	68.7
R11	300 (0)	15 (1)	2 (−1)	12.1
R12	300 (0)	15 (1)	12 (1)	10.0
R13	300 (0)	10 (0)	7 (0)	17.0
R14	300 (0)	10 (0)	7 (0)	16.7
R15	300 (0)	10 (0)	7 (0)	17.2

The solutions were prepared by adding 50 mL of the concentration, mass of GO, and pH into an Erlenmeyer flask (Table 1). The adsorption system was assembled with deionized water and 1% Tween 80 in solution placed in a Tecnal TE-4200 Shaker for 24 h at 25 °C and 50 rpm. The absorbance was measured at nanometric wavelength 254 [29] in the UV-VIS Global Analyzer (São Paulo, Brazil). The pHs were adjusted during adsorption with molar solutions, the shame methodology pHpzc, using aliquots every 3 h throughout the adsorption process [20,30]. The final concentration (C_{Final}) was calculated from the UV-VIS calibration relating to absorbance and butylparaben concentration, and then the *ER*% was calculated using Equation (2).

$$ER\,(\%) = \left(1 - \frac{C_{Final}}{C_{initial}}\right) \times 100 \tag{2}$$

The adsorption kinetics were obtained for the best condition in Table 1, and the mass quantity of adsorption at equilibrium (Q_e = µg·g^{-1}) was determined from Equation (3).

$$Q_e = \frac{(C_0 - C_e) \times V}{m} \tag{3}$$

where *Ce* is the concentration of the pollutant at equilibrium given in µg·L^{-1}, *V* (L) is the total volume of the solution presented in liters, and m is given in grams of the adsorbent. The Erlenmeyer flasks were added to the Tecnal Shaker under the conditions used in the previous section. The kinetics were obtained within 15 min to 1440 min, and an aliquot of 10 mL was collected, filtered, and measured in UV-VIS. After measurement and conversion into concentration, the experimental data was fitted using PFO Equation (4) and PSO Equation (5), ELC Equation (6), and IPD Equation (7) [31,32] to predict the adsorption of solid–liquid systems [7,10,33,34].

$$\frac{dQ}{dt} = k_1 \times (Q_e - Q_t) \tag{4}$$

$$\frac{dQ}{dt} = k_2 \times (Q_e - Q_t)^2 \tag{5}$$

$$\frac{dQ}{dt} = \alpha \times e^{-\beta \times Q_t} \tag{6}$$

$$Q_t = k_{id} \times t^{0.5} \tag{7}$$

The amount of BP adsorbed at the instant of time is defined as Q_t ($\mu g \cdot g^{-1}$), and the constants of the models are described as k_1 (min^{-1}) for the PFO model and as k_2 ($\mu g \cdot mg^{-1} \cdot min^{-1}$) for the PSO model, α is the initial rate of adsorption ($\mu g \cdot g^{-1} \cdot min^{-1}$), β is the desorption constant ($\mu g \cdot mg^{-1}$) during an experiment, k_{id} is the intraparticle diffusion rate constant ($\mu g \cdot mg^{-1} \cdot h^{-0.5}$) and can be taken as a rate factor (% removed per unit time); it should be noted that Equation (7) represents a simplistic approximation of pore diffusion kinetics without considering the possible impacts of pore dimensions [32].

The experiment determined the equilibrium isotherms in the 0–120 $\mu g \cdot L^{-1}$ concentration range. The experiment was carried out under the same parameters as before and after measuring the absorbance and converting it into C_e and Q_e. Next, C_{eq} was plotted against Q_e, and the Langmuir (Equation (8)) and Freundlich (Equation (9)) models were adjusted using the experimental equilibrium data.

$$Q_e = \frac{Q_{max} \times K \times C_e}{1 + K \times C_e} \tag{8}$$

$$Q_e = K_F \times C^{1/n} \tag{9}$$

Equation (8) has parameters Q_{max} ($\mu g \cdot g^{-1}$) and K ($L \cdot mg^{-1}$), which represent the adsorptive capacity and affinity of the adsorbate. Equation (9), Freundlich, refers to the adsorption of the adsorbate on multilayers and energetically heterogeneous surfaces, where K_F ($\mu g \cdot g^{-1} \cdot L^{-1}$) is the Freundlich constant, which represents the intensity of adsorption, and n is defined as the energy on the surface of the adsorbent. The models have thermodynamic consistency, and the Langmuir isotherm describes adsorption phenomena that occur on energetically homogeneous surfaces [35].

The temperature effect was used to determine thermodynamic parameters such as enthalpy change (H-kJ·mol^{-1}), entropy change (S-kJ·K·mol^{-1}), and Gibbs free energy (G-kJ·mol^{-1}). The experiments were carried out under the same conditions as the equilibrium isotherms, using three temperatures: 293 K, 325 K, and 341 K [36].

The ionic strength was also evaluated to analyze the electrostatic attractive and repulsive interactions of the adsorption mechanism, which the presence of ions can reduce. The analysis was carried out under the same conditions as the equilibrium isotherms, with only the ionic strength of the aqueous solutions being altered: sodium chloride (NaCl) was added as a supporting electrolyte at 0.01 M, 0.30 M, and 1.00 M [36].

The regeneration protocol was carried out after completion of the adsorption process following the BP kinetic process [30,37]. The functional material was collected, centrifuged, and washed, and then 30 mL of 99.6% pure analytical grade ethanol was added at 20 ± 1 °C for 5 h to desorb the pollutant. Finally, the sorbent was regenerated and washed with deionized water for reuse over 5 cycles.

2.4. Evaluation of the Toxic of BP in Aqueous Media Before and After Adsorption

The BP phytotoxicity analysis was carried out on *A. cepa* bulbs before and after using the GO adsorbent. The *A. cepa* bulbs used in the toxicity analysis were obtained from an organic garden and were free of synthetic fertilizers and pesticides. The dried cataphylls were removed, and the bulbs were washed in distilled water. After preparing the BP solutions at concentrations of 30 and 600 $\mu g \cdot L^{-1}$, the cleaned bulbs were placed in contact with the solutions for 120 h (five days). Likewise, after adsorbing the paraben solutions, other clean bulbs were placed in contact with the obtained solutions for 120 h for rooting. Five onions (replications) were used for each analysis [7,10].

The cytotoxicity and genotoxicity analyses followed the same procedure before and after adsorption with the adsorbent [7,10,38]. However, five roots were collected in Carnoy solution, 3 parts methanol to 1 part acetic acid, for 20 h. After this, the roots were washed three times with distilled water, soaked in a 1 N HCl solution for 15 min, and then washed three times with distilled water. The meristematic was macerated and stained with 2% acetic orcein to prepare the slides and analyzed with an optical microscope using a 40× magnification. After analysis, the Mitotic Index (*MI*) was established for each treatment by counting 2000 cells per bulb and 10,000 per treatment. To establish the *MI* (Equation (10)), cells in interphase (which are not dividing) and cells in division (prophase, metaphase, anaphase, and telophase) were counted.

$$MI = \frac{Total\ number\ of\ dividing\ cells}{Total\ number\ of\ cells\ analyzed} \times 100 \qquad (10)$$

The Cell Alteration Index (*CCI*), Equation (11), determined the genotoxic potential of the solutions before and after passing through the GO, evaluating 1000 cells per treatment, in which 200 cells were counted per bulb. The cellular alterations considered were micronuclei, sticky chromosomes, chromosome disorganization in the different stages of mitosis (prophase, metaphase, anaphase, and telophase), chromosome breaks and bridges, and polyploidy. The cell alteration index was calculated as follows:

$$CCI = \frac{Nmero\ de\ alteraes\ celulares}{1000} \times 100 \qquad (11)$$

The cytotoxicity and genotoxicity effects of the different BP treatments on *A. cepa* were analyzed with $p \leq 0.05$ since the Lilliefors test showed that the data obtained were non-normal [7,10].

3. Results and Discussion

3.1. Graphene Oxide Production and Characterization

Figure 1a shows the interaction between the GO and the pH of the solution. The GO shows that the pHpzc was 7.0, neutral [18,39]. The neutral pH indicates that the GO has stabilized positive and negative charges. BP has a pKa of 8.47 [40]. This means that at pH values within this range, it gives up H ions$^+$ to the aqueous solution to form anions. In acidic environments, the BP molecule protonates with H ions$^+$; consequently, neutral molecules are predominate in the solution. In basic environments, however, the surface charge is negative, reducing the molecule's adsorption capacity; electrostatic repulsion occurs between the adsorbent and the adsorbate charges [7].

At pH values close to pHpzc, the difference in surface charges is zero, increasing the interaction between contaminant and adsorbent [41]. The pH ranges reported above can influence the pollutant's adsorption capacity, but the ionic counter-charges in the system are not the only factors that influence the adsorption process.

Thus, this study works at pH values above pHpzc because, in aquatic systems at pH values above pHpzc, the net charge on the surface of GO is negative due to the deprotonation of the carboxyl and hydroxyl groups. As a result, the electrostatic interactions with positively charged BP become more favorable. In contrast, at pH values below pHpzc, the net charge on the GO surface becomes positive, and the electrostatic repulsion between BP and graphene surfaces of the same charge increases [42]. The BET area is a factor that directly influences the adsorption of the pollutant.

Figure 1b shows the data and the analyzed BET. The graph shows that the adsorption–desorption isotherm of GO has an IUPAC type IV classification. This type of classification is given to mesoporous materials with narrow hysteresis, showing a low variation in N_2 adsorption [7,43,44]. According to IUPAC, hysteresis occurs at relative pressures lower than 0.4, as the increase in relative pressure indicates the development of micropores.
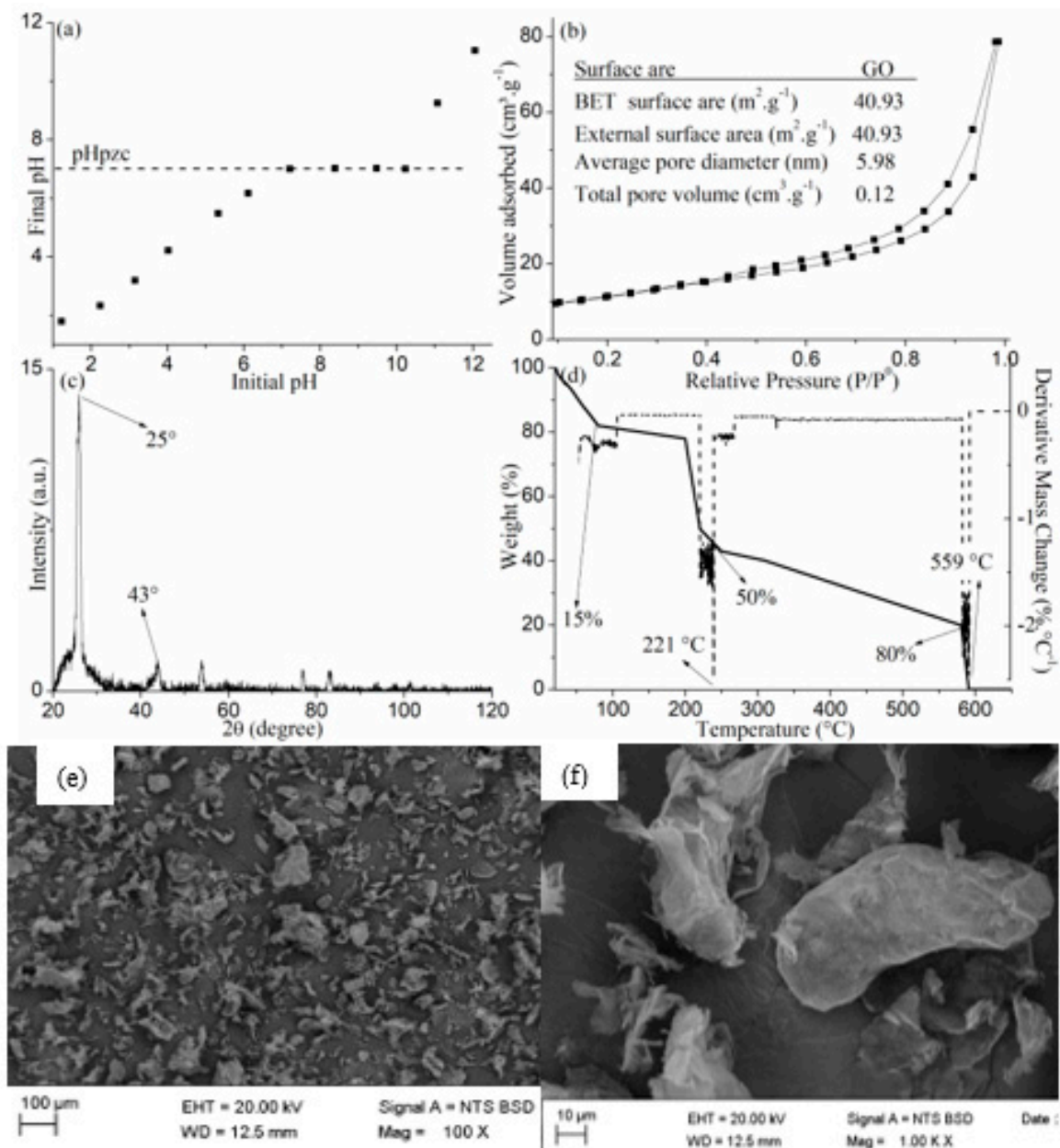
Figure 1. GO characterization chart. (**a**) pHpzc. (**b**) BET. (**c**) XDR. (**d**) TGA/DTG. (**e**,**f**) SEM.

Figure 1b shows the properties of the GO produced in this study. The values found were lower than those found by Vu et al. (2020) [45]. The values obtained were 290 $m^2 \cdot g^{-1}$ and 0.33 $cm^3 \cdot g^{-1}$. In this study, the conversion of mesopores into micropores was not achieved. This may have occurred because SEM and BET analyses were performed to study the surface morphology and surface area of the synthesized compound, and the sheets in the graphite structure were piled on top of each other by weak Van der Waals forces. Using a stirrer at 50 rpm, the graphite sheets may deform and effectively peel off the graphene oxide layers. The expanded layers in graphite are eroded by microjets resulting from bubble eruption [46].

de Assis et al. (2020) [39] obtained a superficial area of 176.00 $m^2 \cdot g^{-1}$ using the Hummers method, as did Moreno-Marenco et al. (2020) [18]. Atheba et al. (2018) [19] also obtained a higher BET surface area than this study, indicating that the material is oxidated, favoring the free surface area. The BET surface area can be influenced by several factors: the acid-base character (pKa) of the functional material, the use of a chemical

activator, as this will generate larger meso- and micropores in the functional material obtained, the degradation of the graphite during the GO formation process, without an inert gas to keep the pores open, which results in the pores closing, or the fact that there is no chemical activator to increase the functional groups in the adsorbent [47]. This may also have occurred due to decreased acids in our GO production procedure. The interactions between BP and GO occurred via chemisorption since HCl, H_2O_2, H_2SO_4, and $KMnO_4$ were used for GO production.

Figure 1c shows the XRD spectrum ranging from 20 to 120°. The spectrum shows a functional material with a more amorphous tendency [48] and a disordered carbon chain [49]. The typical characteristic peak of graphite is assigned at 2θ = 25° with the spacing of ca = 0.35 nm. The graphite peak causes its surface roughness in the graphite layer to stimulate abundant oxygen groups in its boundary layer to bind other molecules [50]. The spectrum of GO reveals its characteristic peak with the Miller plane (001) [51] and (015) [50].

Figure 1c shows the peaks found in the diffractogram, typical of carbonaceous material. The peak at approximately 25° is the characteristic peak of graphite; the intensity of this peak decreases with increasing grinding time [52]. The broadening of the peaks indicates that the spacing rises due to the presence of oxygen atoms and also shows the exfoliation of intermediate layers [53]. The increase in interlayer spacing indicates effective intercalation in the flakes and confirms the formation of GO due to functional groups being dispersed in the plane [54]. Graphite and GO indicate a heterogeneous structure that is not completely oxidized and is composed of graphitic and non-oxidized domains. Diffraction at 43° indicates stacked, crystalline GO layers [55].

Figure 1d shows the thermal analysis of GO; there were three mass percentage losses: the first loss was 15% in the 80 °C range, the second loss was 50% in the 200 °C to 250 °C range, and the third and final loss was 80% of the material; all losses are related to the thermal degradation of the material. Figure 1d shows the transition points that occurred in the thermal analysis process. The temperature of 221 °C shows the degradation of the material, changing its molecular structure from a solid to another state; in the case of GO, this means that there are losses of oxygen molecules, which means that the lattices of the GO structure, which are connected by sp^2 bonds, will fall apart [56]. This means that the lattices of the GO structure, which are connected by sp^2 bonds, will fall apart, and at a temperature of 559 °C to 650 °C, the GO will be completely combusted.

A sudden temperature change generates a thermal shock, removing functionalities such as water vapor, CO, and CO_2 from the GO network. The evolution of gases generates pressure between two stacked layers of GO, which is the key factor for exfoliation. The residual weights of GO were 20% at 600 °C, which indicates the presence of a fraction of non-volatile components. GO has higher thermal stability, probably due to more ordered, H-bonded, and compacted non-exfoliated graphene sheets, which in turn possibly increases the thermal decomposition temperature of GO [57].

Figure 1e,f shows morphological changes of different magnitudes resulting from the production of GO. These figures present irregular morphology since if an inert gas were used in the GO production process, it could generate a porous material [7]. The prepared GO has sheets of different shapes and sizes, but their thickness is the same. In addition, GO has a layered and laminated structure. Generally, such a shape is observed in GO in the form of layers [58]. GO was exfoliated and deformed as a homogeneous and smooth surface with wrinkled edges through the restacking process to reveal a wavy and rolled layer surface structure [50]. This functional material is similar to that produced by Bezerra de Araujo et al. (2023), in which the GO has no cavities in its interior. Figure 1e,f does not show the micro- and mesopore cavities, which can be characterized as channels on the surface of the untreated GO material rather than pores, given the small surface area calculated from the BET analysis.

Table 2 shows the distribution of functional groups in GO. The table shows that GO has more carboxylic and lactonic groups. The functional material is acidic for these two

functional groups, while the phenolic groups define the materials as essential [7]. The variation in the number of functional groups is related to the reaction time, as we left it around twelve hours, and the number of functional groups is consistent with the number of functional groups. In the study by Kumar and Srivastava (2018) [59], the carboxylic and lactonic groups increase in proportion to the increase in GO reaction time due to the oxidation of some of the hydroxyl groups into carbonyl groups and the loss of water molecules from the carboxylic molecules and phenol groups at the ends of the GO sheets.

Table 2. Titration results using the Boehm method and FRX.

Parameters Boehm GO	m_{eq} (mmol·g^{-1})
Carboxylic	4.751
Lactonics	2.231
Phenolics	0.000
Basic	0.000
Elemental analysis	**GO %**
C	50.29
O	47.05
H	2.42
$C_{110}H_{45}O_{23}$	99.76
Other Components	0.24

The elemental analysis of the GO composite was carried out using XRF analysis (Table 2). The combustion and pyrolysis process detected carbon, hydrogen, and oxygen determination. The values are similar to those obtained by Vu et al. (2020) [45] and Peña-Benítez et al. (2016) [60], showing the presence of small amounts of materials added to C, H, and O due to the Hummers-type process.

3.2. Adsorption

The Box–Behnken design (Table 1) was applied to optimize the *ER*, and the results showed considerable information and reaffirmed the usefulness of the statistical design for conducting experiments. RSM optimization was used to determine the levels of these factors. The mathematical relationship of coefficients and *p*-values is listed in Table 3 for the measured responses. Coefficients with a *p*-value of less than 0.05 significantly affected the model's predictive efficiency for the measured response. The polynomial Equation relating to the *ER*% response follows:

$$ER\% = 30.818 + 60.880 \times x_1 \tag{12}$$

Table 3. Significance test and standard error of the ER%. Combined regression variables were analyzed for concentration.

Parameters	Effects	Standard-Error	*p*-Value
A	30.818	6.063	0.00382
x_1	60.880	7.425	0.00936
x_1^2	−6.167	5.465	0.597
x_2	−21.740	7.425	0.203
x_2^2	−18.077	5.465	0.159
x_3	−0.7402	0.074	0.962
x_3^2	3.4724	5.465	0.763
$x_1.x_2$	−2.4289	6.501	0.912
$x_1.x_3$	−17.030	10.501	0.454
$x_2.x_3$	−17.650	10.501	0.439

Equation (12) shows that the factors pollutant concentration (x_1), adsorbent concentration (x_2), and pH (x_3) are related to the effect on the response variable *ER*%. Coefficients

with more than one factor or those with more extensive terms represent interaction terms and quadratic relationships, respectively (Table 3).

Analyzing the *p*-value of the coefficients in Equation (12), the only factor considered significant was x_1. This can be seen in Figure 2, where the response variable *ER*% is correlated with the factors tested. Figure 2a shows that the pollutant concentrations between 600 and 700 μg·L^{-1} obtained a higher *ER*% than the experiments conducted at other concentrations. Figure 2b shows that pH between 7 and 12 also influenced the increase in *ER*%. In contrast, Figure 2c shows that at concentrations between 600 and 700 μg·L^{-1} and any pH range, there is an increase in *ER*%.
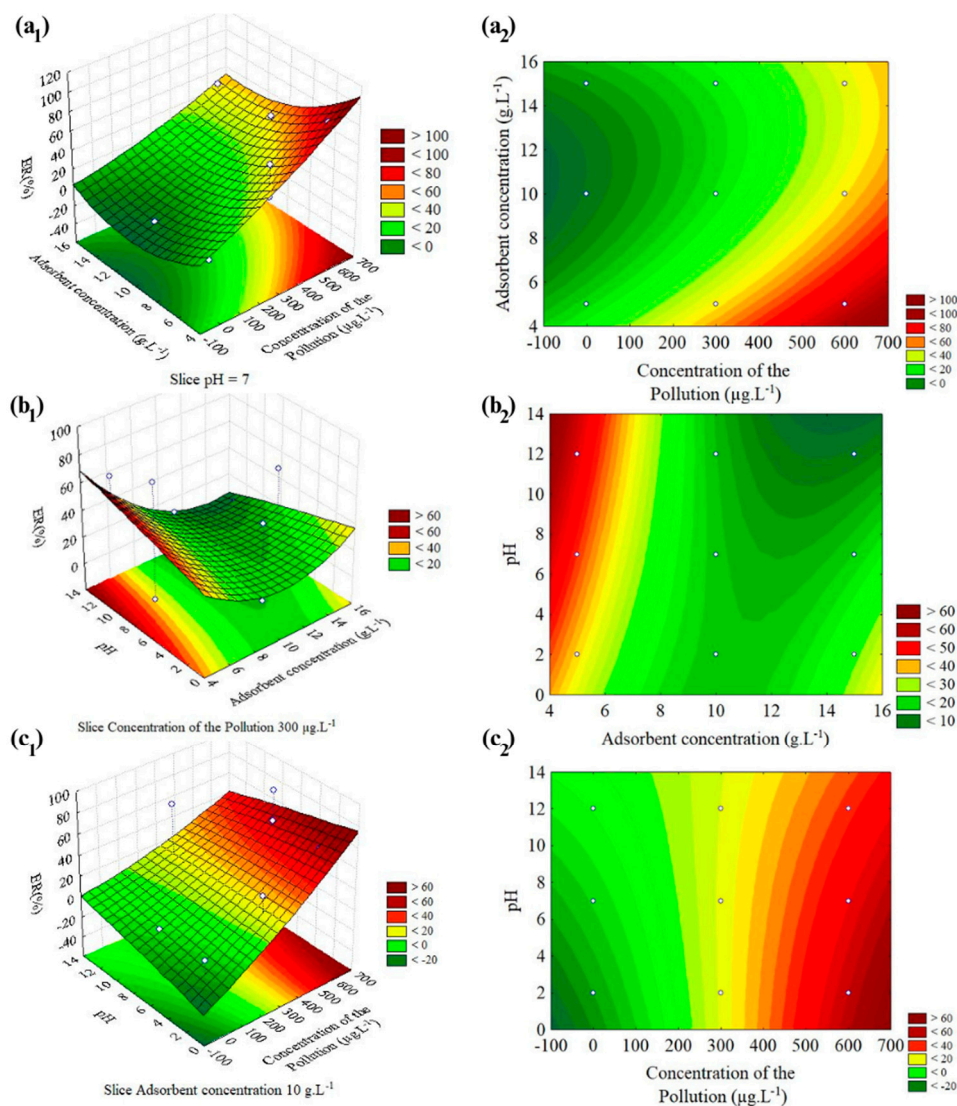

Figure 2. RSM and contours of the butylparaben and GO.

The best adsorption process conditions evaluated for the BP/GO system were R3-84.9%, conducted at 600 μg·L^{-1}, adsorbent concentration 5 g·L^{-1}, and pH 7, respectively. The higher *ER*% may be correlated with a better mass transfer until complete adsorption between the pollutant and the adsorbent because, for high concentrations, such as the R3 run, the adsorption processes at high concentrations requires less time for the adsorptive capacity to remain constant [61]. Atheba et al. (2018) achieved 95% *ER*% for pH 7 and 4 g·L^{-1}, for adsorbent concentrations of 1 g·L^{-1}; the efficiency was 45%.

GO is driven by hydrophobic, H-bonding, electrostatic, and π–π interactions [62]. Species such as BP are hydrophobic pollutants that must be effectively removed, especially

adsorbents based on hydrophobic graphene, which has a high surface area and strong hydrophobicity; graphene is a potential candidate for removing parabens from water. However, the adsorption of parabens by graphene and the related adsorption mechanism have not been reported without additives [17]. The interactions of the BP adsorption process with GO were considered as reactions with radicals and non-radicals [7,10,63–66]. The aqueous solution releases the OH ion$^-$ which interacts with pollutants to form intermediates. The O_2 groups on the surface of the functional material generate this interaction. A mesomeric effect on the carbon double bond is where the carbon double bond moves to the oxygen bond, forming the carbon cation and the oxygen anion. Then, this interaction around the carbon moves to the carbon attached to the OCH_3. This mesomeric effect causes adsorption between the molecule and the GO. The OH^- groups contribute to redox reactions and electron transfer in mesomeric effects. The GO electrons interact with the BP and increase the electron transfer capacity through π electrons, carrying out the adsorption process [63]. The adsorption kinetics used the R3 run to perform the adsorption kinetics with the functional material used in this study.

Figure 3a,b shows the behavior of the experimental data according to time, the PFO (Equation (4)), PSO (Equation (5)), ELC (Equation (6)), and IPD (Equation (7)), used to model the experimental data.
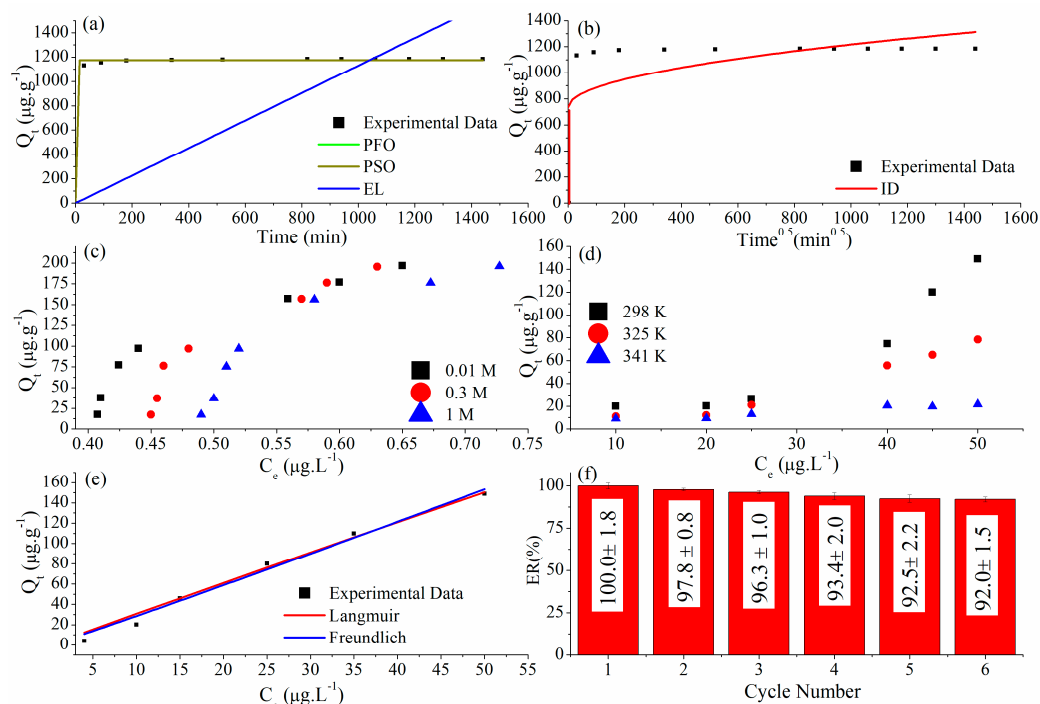

Figure 3. Adsorption data and models. (**a**,**b**) Kinetic. (**c**) Temperatures. (**d**) Ionic strength. (**e**) Isotherms Freundlich model, and the red line represents the model of Langmuir. (**f**) Regeneration of the GO.

The PFO model is the one that phenomenologically depends on the initial concentration to be adsorbed [61]. The PSO model is based on chemisorption, a technique not used in this study, and adsorption is independent of the initial concentration but rather depends on the adsorption capacity of the adsorbent [67]. The ELC model better describes PSO kinetics, assuming the sorbent surface is energetically heterogeneous. The model is also used for the chemisorption of gases on heterogeneous adsorbent surfaces [68]. For porous adsorbents, the IPD of the adsorbate molecules or ions in the pores must also be considered to find a suitable kinetic model for the adsorption process. In many cases, intraparticle diffusion can control the absorption rate of an adsorbate [32].

The adsorption process took around 800 min to stabilize the adsorption rate, which increased exponentially until this time. This shows that the number of adsorption sites

available on this functional material has reached equilibrium, indicating the GO's saturation. Instant adsorption occurs in the adsorbent layer, followed by intraparticle diffusion at slower adsorption rates [8], as noted in the data in this study. Table 4 shows the adsorption kinetic parameters obtained from the fitting curves and the amount of BP adsorbed on the GO, calculated experimentally.

Table 4. Parameters are kinetic and are isotherms of the equilibrium of butylparaben adsorption isotherms on GO.

Model	Parameters Kinetic	
	Parameter	Value
PFO	Q_e (µg·g^{-1})	657.00 ± 8.99
	k_1 (min^{-1})	0.003 ± 0.001
	Adj. R-Square	0.995
PSO	Q_e (µg·g^{-1})	486.09 ± 20.10
	k_2 (µg·g^{-1}·min^{-1})	0.102 ± 0.08
	Adj. R-Square	0.229
ELC	α (µg·g^{-1}·min^{-1})	0.573 ± 0.065
	β (µg·g^{-1})	1.742 ± 0.021
	Adj. R-Square	0.658
IPD	C (µg·g^{-1})	−5.48 ± 0.065
	k_{di} (min$^{-0.5}$)	19.33 ± 1.43
	Adj. R-Square	0.942
Isotherms	Parameters Isotherms of the equilibrium	
Langmuir	Qmax (µg·g^{-1})	2432 ± 15.07
	K (L·g^{-1})	0.008 ± 0.001
	Adj. R-Square	0.999
Freundlich	K_f (µg·g^{-1}·L$^{-1/n}$)	50.54 ± 1.58
	n	1.52 ± 0.15
	Adj. R-Square	0.982

The correlation coefficients (R^2) showed values of 0.995 for the PFO, 0.229 for the PSO, 0.658 for the ELC model, and 0.942 for the IPD model. From the models tested, the variables found are defined as follows: Q_e is the amount of BP adsorbed at equilibrium given in µg·g^{-1}; t is the time given in minutes; k_1 is the adsorption rate constant, the unit being defined as the inverse of the time in minutes; k_2 is the intraparticle diffusion rate constant defined as µg·g^{-1}·min^{-1}; α is the initial adsorption rate given in µg·g^{-1}·min^{-1}; β is the desorption constant µg·g^{-1} during an experiment; k_{id} [µg·g^{-1}·h$^{-0.5}$] is the intraparticle diffusion rate constant [67].

The model that best fitted the experimental data was the PFO model. As mentioned, this model phenomenologically depends on the initial concentration to be adsorbed [61]. The model converges to the run used in this study, which is best used for high initial concentrations and has some active sites on the adsorbent [7,10]. The low correlation can justify the PSO and ELC order model because the model is based on chemisorption, a technique not used in this study, and adsorption is independent of the initial concentration rather than the adsorption capacity of the adsorbent [67]. The intraparticle diffusion model also showed a good correlation, showing the BP molecule's diffusion in the GO adsorbent.

The equilibrium isotherm and the Langmuir and Freundlich models were carried out (Figure 3b). Both models showed a good quadratic correlation, 0.992 for the Langmuir model and 0.982 for the Freundlich model. This is important for interpreting adsorption systems and understanding liquid–solid interface mechanisms [67].

Figure 3b was plotted between the contraction ranges 0 µg·L^{-1} to 120 µg·L^{-1} [69]. The Langmuir model was calculated using Equation (8), and the Freundlich model using Equation (9). Figure 3b shows a tendency towards stabilization for higher concentrations. The

Langmuir model is used for monolayer adsorption, atmospheric pressure, homogeneous systems, and constant temperature, and the process stabilizes due to the saturation of the adsorbent [70]. Table 4 shows the high value of Q_{max}, which means that graphene's surface area, pore volume, particle size distribution, and multilayer development are greater than those of commercial carbon [7]. The Freundlich model shows that n greater than zero indicates that the adsorption process was spontaneous [7,10,67]. Several studies with different adsorbents have demonstrated that the Langmuir model represents the experimental data more quickly than the Freundlich model [3,17–19].

Temperature analysis is also a key factor in adsorption, as the adsorption capacity changes with temperature variation [36]. Figure 3c shows that BP reaches a maximum adsorption capacity of 661.72 µg·g^{-1} (341 K) and 524.53 µ·g^{-1} (298 K). The results show that adsorption is an endothermic process considering different adsorbate–adsorbent systems [71,72]. The Gibbs free energy (ΔG°) is also related to the equilibrium constant K_{eq} (L·mol^{-1}). The enthalpy variation (ΔH°) and entropy variation (ΔS°) values are calculated from Equations (13)–(15).

$$\Delta G° = \Delta H° - Tx\Delta S° \tag{13}$$

$$\Delta G° = -RTx\ln K_{eq} \tag{14}$$

$$\ln K_{eq} = -\frac{\Delta H°}{RT} + \frac{\Delta S°}{R} \tag{15}$$

This method determined the adsorption equilibrium constants. The values of K_{eq} are obtained by plotting a straight line of $\ln(Q_t \cdot Ce^{-1})$ as a function of Q_t based on a least squares analysis and extrapolating Q_t to 0. The intersection of the horizontal axis gives the value of K_{eq}. A Van't Hoff graph produces a straight line of $\ln K_{eq}$ as a function of (1T^{-1}). The variations of ΔH° and ΔS° were calculated from the slope and intercept of the graph, respectively [36]. Adsorption occurs in multilayers on the GO adsorbent. Table 5 shows negative ΔG values, which indicates that the adsorption process is thermodynamically spontaneous.

Table 5. Parameters thermodynamics calculated for BP adsorption isotherms on GO and mitotic and cellular indices.

Parameters Thermodynamic			
T (K)	**ΔH (kJ·mol^{-1})**	**ΔS (kJ·K^{-1}·mol^{-1})**	**ΔG (kJ·mol^{-1})**
293	2.436	3.24·10^{-2}	−7.064
325	-	-	−8.101
341	-	-	−8.621

Mitotic indices and cellular alteration indices of root meristems of *Allium cepa* L.			
Treatment	**Concentration of the BP**	**MI/SD (%)**	**ICC/SD (%)**
	CO	100.00 ± 0.8	0.1 ± 0.9
Before adsorption	30 µg·L^{-1}	59.1 ± 0.5 *	17.4 ± 0.6 *
	600 µg·L^{-1}	59.0 ± 0.8 *	38.9 ± 0.9 *
After adsorption with graphene	600 µg·L^{-1}	89.5 ± 1.0	0.1 ± 1.1

Notes: CO: distilled water control, MI: Mitotic Index, ICC: Index of Cellular Changes, SD: standard deviation. For MI, data are expressed as a percentage of CO values. * Significantly different from the CO, according to the Kruskal–Wallis test followed by Dunn's post hoc test ($p \le 0.05$).

The positive ΔH° value also indicates that the nature of the adsorption process is endothermic. The increase in the value of the adsorbed capacity of the adsorbent with increasing temperature also supports this. The positive value of ΔS° shows the increase in randomness at the solid–solution interface during the adsorption process [36]. The ΔG

found in this study is spontaneous compared to that found by Atheba et al. (2018) and lower than that found by Moreno-Marenco et al. (2020) [18]. However, both studies have $\Delta S°$ higher than the endothermic process, which explains why the degree of randomness at the solid–liquid interface increased during the adsorption of BP on GO.

The effect of ionic strength on BP adsorption was studied at pH 7.0 in GO, where the adsorbent and pollutant have opposite charges (pH_{PZC} = 7.00 and pKa = 8.47). This situation can be confirmed with the speciation diagram in Figure 3d, where more than 99% of the butylparaben is presented in the anionic form. The isotherms were carried out with three different NaCl solutions at concentrations of 0.01 M, 0.30 M, and 1.00 M (Figure 3d). All the experiments were conducted under the same conditions as the equilibrium isotherms.

The effect of ionic strength on strength is shown in Figure 3d; for all concentrations analyzed, the adsorption capacity remained constant with increasing equilibrium concentration. The increase in NaCl produces an increase in the repulsive interactions between the adsorbate and the adsorbent due to the deprotonation of the BP and the increase in the negative charge density on the surface of the GO. Theoretically, when the electrostatic forces between the adsorbent surface and the adsorbed ions are attractive, an increase in ionic strength will decrease the adsorption capacity. When the electrostatic attraction is repulsive, an increase in ionic strength will increase adsorption [36]. Therefore, in this case, the concentration of 1 M obtains the best results because a curve with higher Ce was obtained for the same adsorption capacity.

To evaluate the effectiveness of the GO adsorbent, the five regeneration cycles were analyzed (Figure 3f) [30,37]. The regeneration and reuse of the adsorbent were carried out under the best BP adsorbed concentration conditions described above. GO shows a high removal efficiency after two recycling stages. The GO removal proficiency in the first cycle was 89.2% $\pm$ 1.5% and that in the second cycle was 84.9% $\pm$ 1.3%. From the third cycle onwards, there was a decrease in removal proficiency, which changes the desorption capacity. Compared to the study by Shoushtarian et al. [73], who used GO, this study obtained a shorter regeneration cycle in the first two stages and an efficiency of 58.06% in the fourth cycle. It can be concluded that GO is efficient when it is used for up to two regenerations.

3.3. Evaluation of the Toxic of BP in Aqueous Media Before and After Adsorption

The *A. cepa* bioassay is used worldwide as a model for assessing the toxicity of organic and inorganic pollutants at the cellular level. It has high sensitivity, even when the concentrations of these compounds in water are in the nanogram range, and the results obtained have a significant correlation with those obtained with animals, other plants, and in vitro [74]. Currently, the *A. cepa* test system has been used to validate the efficiency of adsorbents in removing emerging pollutants and herbicides from the aqueous medium [10,75].

Based on the results in Table 5, concentrations of 30 and 600 $\mu g \cdot L^{-1}$ caused significant cytotoxicity and genotoxicity to *A. cepa* root meristems before adsorption. These results are analogous to Todorovac et al. (2021) [76], who observed the broad cytotoxicity of this contaminant to *A. cepa* roots and human lymphocytes.

In contrast, inhibition of cell division and significant cell changes were no longer observed after the adsorption of BP solutions by the three adsorbents evaluated, indicating that they efficiently removed butylparaben from the aqueous solution.

Some studies have explored BP adsorption processes using various adsorbents. Wei et al. [17] reported a low *ER*% for parabens on graphene oxide, close to 20% at pH 6, with an adsorbent concentration of 400 $mg \cdot L^{-1}$ and a pollutant concentration of 40 $mg \cdot L^{-1}$. Moreno-Marenco et al. [18], using the shell of the African oil palm (*Elaeis guineensis*) chemically modified with calcium chloride and magnesium chloride solutions at different concentrations, observed a negative enthalpy of immersion, indicating the exothermic nature of the adsorption process.

Correa-Navarro et al. [3] synthesized benzoic and magnetic cellulose for BP removal. Magnetic cellulose's maximum BP adsorption capacity was 12.03 mg·g^{-1}, with the best kinetic models being PFO and PSO compared to EL, Weber, Morris, and Boyd. Langmuir's adsorption isotherm model performed better than Freundlich's and Sips's. Atheba et al. [19] used low-cost activated carbon derived from coconut biochar for BP adsorption, achieving an *ER*% greater than 97% at pH 7. The equilibrium data were fitted to the Langmuir, Freundlich, and Temkin isotherm models, with a correlation coefficient greater than 0.9 for the tested isotherms. Based on the analyses conducted, it can be concluded that this system is promising since, considering the removal efficiency and adsorption capacity, this study presented higher values than those reported in this study.

4. Conclusions

This study investigated the characterization of GO from solid graphite. Based on our analysis, GO showed a mass loss in line with other studies, lower surface area, neutral electronegativity, pH 7, and was composed of functional groups formed by hydroxyls, carbonyls, and aromatic rings. The removal efficiency values of the BP system with GO were close to 84.2%.

The kinetic data revealed that the adsorption rate follows the PFO model, suggesting that adsorption occurs around 800 min and reaches equilibrium at slower rates for all initial BP concentrations. The adsorption equilibrium was also evaluated, showing that the Langmuir model best represents the results based on environmental conditions. The temperature effect showed that the adsorption process is spontaneous with a negative Gibbs energy value, and the ion effect showed that a low electronegativity difference does not increase the pollutant's adsorption capacity. Regeneration was efficient up to the second cycle.

Based on these facts, it can be concluded that the adsorption process carried out, with BP contaminant and GO adsorbent, is efficient on a laboratory scale, as the ecotoxicity studies on *A. cepa* confirmed the efficiency of BP removal in aqueous media, validating the entire adsorption process used to remove the pollutant in aqueous media.

Author Contributions: Conceptualization, L.C.-F., A.P.P. and O.V.J.; methodology, E.B.; validation and data curation, L.M.S.T., E.A.d.A. and D.E.S.; investigation and writing—review and editing, V.J.; writing—original draft preparation, G.L.D.P.; project administration, O.V.J. All authors have read and agreed to the published version of the manuscript.

Data Availability Statement: We declare that all data are in the manuscript. Therefore, the data availability statement does not apply to this study.

Conflicts of Interest: The authors declare no conflicts of interest.

References

1. Xiang, J.; Lv, B.R.; Shi, Y.J.; Chen, W.M.; Zhang, J.L. Environmental Pollution of Paraben Needs Attention: A Study of Methylparaben and Butylparaben Co-Exposure Trigger Neurobehavioral Toxicity in Zebrafish. *Environ. Pollut.* **2024**, *356*. [CrossRef] [PubMed]
2. Vale, F.; Sousa, C.A.; Sousa, H.; Santos, L.; Simões, M. Impact of Parabens on Microalgae Bioremediation of Wastewaters: A Mechanistic Study. *Chem. Eng. J.* **2022**, *442*, 136374. [CrossRef]
3. Correa-Navarro, Y.M.; Rivera-Giraldo, J.D.; Cardona-Castaño, J.A. Modified Cellulose for Adsorption of Methylparaben and Butylparaben from an Aqueous Solution. *ACS Omega* **2024**, *9*, 30224–30233. [CrossRef] [PubMed]
4. Maske, P.; Dighe, V.; Mote, C.; Vanage, G. N-Butylparaben Exposure through Gestation and Lactation Impairs Spermatogenesis and Steroidogenesis Causing Reduced Fertility in the F1 Generation Male Rats. *Environ. Pollut.* **2020**, *256*, 112957. [CrossRef]
5. Pereira, A.R.; Simões, M.; Gomes, I.B. Parabens as Environmental Contaminants of Aquatic Systems Affecting Water Quality and Microbial Dynamics. *Sci. Total Environ.* **2023**, *905*, 167332. [CrossRef]

6. Medkova, D.; Hollerova, A.; Riesova, B.; Blahova, J.; Hodkovicova, N.; Marsalek, P.; Doubkova, V.; Weiserova, Z.; Mares, J.; Faldyna, M.; et al. Pesticides and Parabens Contaminating Aquatic Environment: Acute and Sub-Chronic Toxicity towards Early-Life Stages of Freshwater Fish and Amphibians. *Toxics* **2023**, *11*, 333. [CrossRef] [PubMed]

7. Rocha, B.C.d.S.; de Moraes, L.E.Z.; Santo, D.E.; Peron, A.P.; de Souza, D.C.; Bona, E.; Valarini, O. Removal of Bentazone Using Activated Carbon from Spent Coffee Grounds. *J. Chem. Technol. Biotechnol.* **2024**, *99*, 1342–1355. [CrossRef]

8. do Nascimento, R.F.; de Lima, A.C.A.; Vidal, C.B.; Melo, D.d.Q.; Raulino, G.S.C. *Adsorção: Aspectos Teóricos e Aplicações Ambientais*; Imprensa Universitária: Fortaleza, Brazil, 2020; p. 308.

9. Ribas, F.B.T.; da Silva, W.L. Biosorption: A Review of Promising Alternative Methods in Wastewater Treatment. *Rev. Mater.* **2022**, *27*, e13212. [CrossRef]

10. da Rocha, S.A.F.; Rocha, B.C.d.S.; de Moraes, L.E.Z.; Villaça, J.M.P.; Scapin, D.; Santo, D.E.; Gonzalez, R.d.S.; Junior, O.V.; Peron, A.P. Evaluation and Simulation of the Adsorption Capacity of Octocrylene Sunscreen on Commercial Carbon and Biochar from Spent Coffee Beans. *Processes* **2024**, *12*, 1249. [CrossRef]

11. Qu, H.J.; Huang, L.J.; Han, Z.Y.; Wang, Y.X.; Zhang, Z.J.; Wang, Y.; Chang, Q.R.; Wei, N.; Kipper, M.J.; Tang, J.G. A Review of Graphene-Oxide/Metal–Organic Framework Composites Materials: Characteristics, Preparation and Applications. *J. Porous Mater.* **2021**, *28*, 1837–1865. [CrossRef]

12. De Araujo, C.M.B.; De Assis Filho, R.B.; Baptisttella, A.M.S.; Do Nascimento, G.F.O.; Da Costa, G.R.B.; Carvalho, M.N.; Ghislandi, M.G.; Sobrinho, M.A.D.M. Systematic Study of Graphene Oxide Production Using Factorial Design Techniques and Its Application to the Adsorptive Removal of Methylene Blue Dye in Aqueous Medium. *Mater. Res. Express* **2018**, *5*, 065042. [CrossRef]

13. Bezerra de Araujo, C.M.; Wernke, G.; Ghislandi, M.G.; Diório, A.; Vieira, M.F.; Bergamasco, R.; Alves da Motta Sobrinho, M.; Rodrigues, A.E. Continuous Removal of Pharmaceutical Drug Chloroquine and Safranin-O Dye from Water Using Agar-Graphene Oxide Hydrogel: Selective Adsorption in Batch and Fixed-Bed Experiments. *Environ. Res.* **2023**, *216*, 114425. [CrossRef] [PubMed]

14. Peng, W.; Li, H.; Hu, Y.; Liu, Y.; Song, S. Does Silicate Mineral Impurities in Natural Graphite Affect the Characteristics of Synthesized Graphene? *Mater. Res. Bull.* **2016**, *74*, 333–339. [CrossRef]

15. Velusamy, S.; Roy, A.; Sundaram, S.; Kumar Mallick, T. A Review on Heavy Metal Ions and Containing Dyes Removal Through Graphene Oxide-Based Adsorption Strategies for Textile Wastewater Treatment. *Chem. Rec.* **2021**, *21*, 1570–1610. [CrossRef] [PubMed]

16. Andelkovic, I.B.; Kabiri, S.; Tavakkoli, E.; Kirby, J.K.; McLaughlin, M.J.; Losic, D. Graphene Oxide-Fe(III) Composite Containing Phosphate—A Novel Slow Release Fertilizer for Improved Agriculture Management. *J. Clean. Prod.* **2018**, *185*, 97–104. [CrossRef]

17. Wei, Y.; Liu, X.; Wang, Z.; Chi, Y.; Yue, T.; Dai, Y.; Zhao, J.; Xing, B. Adsorption and Catalytic Degradation of Preservative Parabens by Graphene-Family Nanomaterials. *Sci. Total Environ.* **2022**, *806*, 150520. [CrossRef] [PubMed]

18. Moreno-Marenco, A.R.; Giraldo, L.; Moreno-Piraján, J.C. Adsorption of N-Butylparaben from Aqueous Solution on Surface of Modified Granular Activated Carbons Prepared from African Palm Shell. Thermodynamic Study of Interactions. *J. Environ. Chem. Eng.* **2020**, *8*, 103969. [CrossRef]

19. Atheba, P.; Allou, N.B.; Drogui, P.; Trokourey, A. Adsorption Kinetics and Thermodynamics Study of Butylparaben on Activated Carbon Coconut Based. *J. Encapsulation Adsorpt. Sci.* **2018**, *8*, 39–57. [CrossRef]

20. Milonjić, S.K.; Kopečni, M.M.; Ilić, Z.E. The Point of Zero Charge and Adsorption Properties of Natural Magnetite. *J. Radioanal. Chem.* **1983**, *78*, 15–24. [CrossRef]

21. Allwar, A. Characteristics of Pore Structures and Surface Chemistry of Activated Carbons by Physisorption, Ftir And Boehm Methods. *IOSR J. Appl. Chem.* **2012**, *2*, 9–15. [CrossRef]

22. Galvan, D.; Bona, E. Aplicativo Gamma-Gui: Uma Interface Gráfica Amigável Para Planejamento De Experimentos No Matlab. *Quim. Nova* **2024**, *47*, e-20240005. [CrossRef]

23. Valarini Junior, O.; Reitz Cardoso, F.A.; Machado Giufrida, W.; de Souza, M.F.; Cardozo-Filho, L. Production and Computational Fluid Dynamics-Based Modeling of PMMA Nanoparticles Impregnated with Ivermectin by a Supercritical Antisolvent Process. *J. CO2 Util.* **2020**, *35*, 47–58. [CrossRef]

24. Lopes, G.d.S.; de Araujo, P.C.C.; da Silva, M.J.; Paim, L.L.; de Oliveira, K.R.; Valarini Junior, O.; Favareto, R.; Parizi, M.P.S.; Ferreira-Pinto, L. Kinetic Study of Peanut Seed Oil Extraction with Supercritical CO_2. *Res. Soc. Dev.* **2022**, *11*, e15511427098. [CrossRef]

25. Montgomery, D.C. *Design and Analysis of Experiments*, 8th ed.; Wiley: Hoboken, NJ, USA, 2012; Volume 2, ISBN 9781118146927.

26. Debien, I.C.N.; Vardanega, R.; Santos, D.T.; Meireles, M.A.A. Pressurized Liquid Extraction as a Promising and Economically Feasible Technique for Obtaining Beta-Ecdysone-Rich Extracts from Brazilian Ginseng (Pfaffia Glomerata) Roots. *Sep. Sci. Technol.* **2015**, *50*, 1647–1657. [CrossRef]

27. Dean, J.R. Pressurized Liquid Extraction. In *Extraction Techniques for Environmental Analysis*; Wiley: Hoboken, NJ, USA, 2022; pp. 171–204. [CrossRef]

28. Derisso, C.R.; Pompei, C.M.E.; Spadoto, M.; da Silva Pinto, T.; Vieira, E.M. Occurrence of Parabens in Surface Water, Wastewater Treatment Plant in Southeast of Brazil and Assessment of Their Environmental Risk. *Water Air Soil Pollut.* **2020**, *231*, 468. [CrossRef]

29. Rasyid, N.Q.; Muawanah, R. Konsentrasi Pengawet Paraben Pada Produk Perawatan Tubuh. In *Seminar Nasional Hasil Penelitian & Pengabdian Kepada Masyarakat (SNP2M)*; Makassar, 2017; pp. 83–86. Available online: https://jurnal.poliupg.ac.id/index.php/snp2m/article/view/300 (accessed on 12 November 2024).

30. Zbair, M.; El Hadrami, A.; Bellarbi, A.; Monkade, M.; Zradba, A.; Brahmi, R. Herbicide Diuron Removal from Aqueous Solution by Bottom Ash: Kinetics, Isotherm, and Thermodynamic Adsorption Studies. *J. Environ. Chem. Eng.* **2020**, *8*, 103667. [CrossRef]

31. Musah, M.; Azeh, Y.; Mathew, J.; Umar, M.; Abdulhamid, Z.; Muhammad, A. Adsorption Kinetics and Isotherm Models: A Review. *Caliphate J. Sci. Technol.* **2022**, *4*, 20–26. [CrossRef]

32. Sen Gupta, S.; Bhattacharyya, K.G. Kinetics of Adsorption of Metal Ions on Inorganic Materials: A Review. *Adv. Colloid Interface Sci.* **2011**, *162*, 39–58. [CrossRef]

33. Gonçalves Júnior, D.R.; de Araújo, P.C.C.; Simões, A.L.G.; Voll, F.A.P.; Parizi, M.P.S.; de Oliveira, L.H.; Ferreira-Pinto, L.; Cardozo-Filho, L.; de Jesus Santos, E. Assessment of the Adsorption Capacity of Phenol on Magnetic Activated Carbon. *Asia-Pac. J. Chem. Eng.* **2022**, *17*, e2725. [CrossRef]

34. Tan, K.L.; Hameed, B.H. Insight into the Adsorption Kinetics Models for the Removal of Contaminants from Aqueous Solutions. *J. Taiwan Inst. Chem. Eng.* **2017**, *74*, 25–48. [CrossRef]

35. Karri, R.R.; Sahu, J.N.; Jayakumar, N.S. Optimal Isotherm Parameters for Phenol Adsorption from Aqueous Solutions onto Coconut Shell Based Activated Carbon: Error Analysis of Linear and Non-Linear Methods. *J. Taiwan Inst. Chem. Eng.* **2017**, *80*, 472–487. [CrossRef]

36. Spaltro, A.; Simonetti, S.; Torrellas, S.A.; Rodriguez, J.G.; Ruiz, D.; Juan, A.; Allegretti, P. Adsorption of Bentazon on CAT and CARBOPAL Activated Carbon: Experimental and Computational Study. *Appl. Surf. Sci.* **2018**, *433*, 487–501. [CrossRef]

37. Milanković, V.; Tasić, T.; Brković, S.; Potkonjak, N.; Unterweger, C.; Bajuk-Bogdanović, D.; Pašti, I.; Lazarević-Pašti, T. Spent Coffee Grounds-Derived Carbon Material as an Effective Adsorbent for Removing Multiple Contaminants from Wastewater: A Comprehensive Kinetic, Isotherm, and Thermodynamic Study. *J. Water Process Eng.* **2024**, *63*, 105507. [CrossRef]

38. Fiskesjö, G. The Allium Test as a Standard in Environmental Monitoring. *Hereditas* **1985**, *102*, 99–112. [CrossRef]

39. de Assis, L.K.; Damasceno, B.S.; Carvalho, M.N.; Oliveira, E.H.C.; Ghislandi, M.G. Adsorption Capacity Comparison between Graphene Oxide and Graphene Nanoplatelets for the Removal of Coloured Textile Dyes from Wastewater. *Environ. Technol.* **2020**, *41*, 2360–2371. [CrossRef] [PubMed]

40. PubChem NIH National Library of Medicine NCBI. Butylparaben. 2023.

41. Zbair, M.; Ainassaari, K.; Drif, A.; Ojala, S.; Bottlinger, M.; Pirilä, M.; Keiski, R.L.; Bensitel, M.; Brahmi, R. Toward New Benchmark Adsorbents: Preparation and Characterization of Activated Carbon from Argan Nut Shell for Bisphenol A Removal. *Environ. Sci. Pollut. Res.* **2018**, *25*, 1869–1882. [CrossRef]

42. Ersan, G.; Apul, O.G.; Perreault, F.; Karanfil, T. Adsorption of Organic Contaminants by Graphene Nanosheets: A Review. *Water Res.* **2017**, *126*, 385–398. [CrossRef] [PubMed]

43. Calvo-Muñoz, E.M.; García-Mateos, F.J.; Rosas, J.M.; Rodríguez-Mirasol, J.; Cordero, T. Biomass Waste Carbon Materials as Adsorbents for CO2 Capture under Post-Combustion Conditions. *Front. Mater.* **2016**, *3*, 23. [CrossRef]

44. Sarker, A.I.; Aroonwilas, A.; Veawab, A. Equilibrium and Kinetic Behaviour of CO$_2$ Adsorption onto Zeolites, Carbon Molecular Sieve and Activated Carbons. *Energy Procedia* **2017**, *114*, 2450–2459. [CrossRef]

45. Vu, T.T.; La, T.V.; Pham, V.T.; Vu, M.K.; Huynh, D.C.; Tran, N.K. Highly Efficient Adsorbent for the Transformer Oil Purification by ZnO/Graphene Composite. *Arab. J. Chem.* **2020**, *13*, 7798–7808. [CrossRef]

46. Arabpour, A.; Dan, S.; Hashemipour, H. Preparation and Optimization of Novel Graphene Oxide and Adsorption Isotherm Study of Methylene Blue. *Arab. J. Chem.* **2021**, *14*, 103003. [CrossRef]

47. Javier Sánchez, A. *Characterization of Activated Carbon Produced from Coffee Residues by Chemical and Physical Activation*; KTH, School of Chemical Science and Engineering: Stockholm, Sweden, 2011; p. 66.

48. Lykoudi, A.; Frontistis, Z.; Vakros, J.; Manariotis, I.D.; Mantzavinos, D. Degradation of Sulfamethoxazole with Persulfate Using Spent Coffee Grounds Biochar as Activator. *J. Environ. Manag.* **2020**, *271*, 111022. [CrossRef] [PubMed]

49. Ntzoufra, P.; Vakros, J.; Frontistis, Z.; Tsatsos, S.; Kyriakou, G.; Kennou, S.; Manariotis, I.D.; Mantzavinos, D. Effect of Sodium Persulfate Treatment on the Physicochemical Properties and Catalytic Activity of Biochar Prepared from Spent Malt Rootlets. *J. Environ. Chem. Eng.* **2021**, *9*, 105071. [CrossRef]

50. Nithya Priya, V.; Rajkumar, M.; Mobika, J.; Linto Sibi, S.P. Alginate Coated Layered Double Hydroxide/Reduced Graphene Oxide Nanocomposites for Removal of Toxic As (V) from Wastewater. *Phys. E Low-Dimens. Syst. Nanostruct.* **2021**, *127*, 114527. [CrossRef]

51. Khan, A.; Kamal, T.; Saad, M.; Ameen, F.; Bhat, S.A.; Khan, M.A.; Rahman, F. Synthesis and Antibacterial Activity of Nanoenhanced Conjugate of Ag-Doped ZnO Nanorods with Graphene Oxide. *Spectrochim. Acta - Part A Mol. Biomol. Spectrosc.* **2023**, *290*, 122296. [CrossRef]

52. Casallas Caicedo, F.M.; Vera López, E.; Agarwal, A.; Drozd, V.; Durygin, A.; Franco Hernandez, A.; Wang, C. Synthesis of Graphene Oxide from Graphite by Ball Milling. *Diam. Relat. Mater.* **2020**, *109*, 108064. [CrossRef]

53. Sharma, S.; Kothiyal, N.C. Comparative Effects of Pristine and Ball-Milled Graphene Oxide on Physico-Chemical Characteristics of Cement Mortar Nanocomposites. *Constr. Build. Mater.* **2016**, *115*, 256–268. [CrossRef]

54. Jose, P.P.A.; Kala, M.S.; Kalarikkal, N.; Thomas, S. Reduced Graphene Oxide Produced by Chemical and Hydrothermal Methods. *Mater. Today Proc.* **2018**, *5*, 16306–16312. [CrossRef]

55. Stobinski, L.; Lesiak, B.; Malolepszy, A.; Mazurkiewicz, M.; Mierzwa, B.; Zemek, J.; Jiricek, P.; Bieloshapka, I. Graphene Oxide and Reduced Graphene Oxide Studied by the XRD, TEM and Electron Spectroscopy Methods. *J. Electron Spectros. Relat. Phenom.* **2014**, *195*, 145–154. [CrossRef]

56. Farivar, F.; Yap, P.L.; Hassan, K.; Tung, T.T.; Tran, D.N.H.; Pollard, A.J.; Losic, D. Unlocking Thermogravimetric Analysis (TGA) in the Fight against "Fake Graphene" Materials. *Carbon* **2021**, *179*, 505–513. [CrossRef]

57. Tohamy, H.A.S.; El-Sakhawy, M.; Kamel, S. Carboxymethyl Cellulose-Grafted Graphene Oxide/Polyethylene Glycol for Efficient Ni(II) Adsorption. *J. Polym. Environ.* **2021**, *29*, 859–870. [CrossRef]

58. Yang, J.; Shojaei, S.; Shojaei, S. Removal of Drug and Dye from Aqueous Solutions by Graphene Oxide: Adsorption Studies and Chemometrics Methods. *npj Clean Water* **2022**, *5*, 5. [CrossRef]

59. Kumar, N.; Srivastava, V.C. Simple Synthesis of Large Graphene Oxide Sheets via Electrochemical Method Coupled with Oxidation Process. *ACS Omega* **2018**, *3*, 10233–10242. [CrossRef]

60. de la Peña-Benítez, P.R.; García-Santos, A.; Santonja, R.; Sapiña, M.; Jiménez-Relinque, E.; Castellote, M.; Sánchez-Cifuentes, M.; de la Peña-Benítez, P.R.; García-Santos, A.; Santonja, R.; et al. Evaluación Ambiental de Pinturas Al Agua Para Exteriores de Los Edificios Modificadas Con Óxido de Grafeno. *Superf. y Vacío* **2016**, *29*, 105–111.

61. Liu, Y.; Shen, L. From Langmuir Kinetics to First- and Second-Order Rate Equations for Adsorption. *Langmuir* **2008**, *24*, 11625–11630. [CrossRef]

62. Liu, F.F.; Zhao, J.; Wang, S.; Du, P.; Xing, B. Effects of Solution Chemistry on Adsorption of Selected Pharmaceuticals and Personal Care Products (PPCPs) by Graphenes and Carbon Nanotubes. *Environ. Sci. Technol.* **2014**, *48*, 13197–13206. [CrossRef] [PubMed]

63. Grilla, E.; Vakros, J.; Konstantinou, I.; Manariotis, I.D.; Mantzavinos, D. Activation of Persulfate by Biochar from Spent Malt Rootlets for the Degradation of Trimethoprim in the Presence of Inorganic Ions. *J. Chem. Technol. Biotechnol.* **2020**, *95*, 2348–2358. [CrossRef]

64. Giannakopoulos, S.; Frontistis, Z.; Vakros, J.; Poulopoulos, S.G.; Manariotis, I.D.; Mantzavinos, D. Combined Activation of Persulfate by Biochars and Artificial Light for the Degradation of Sulfamethoxazole in Aqueous Matrices. *J. Taiwan Inst. Chem. Eng.* **2022**, *136*, 104440. [CrossRef]

65. Mrozik, W.; Minofar, B.; Thongsamer, T.; Wiriyaphong, N.; Khawkomol, S.; Plaimart, J.; Vakros, J.; Karapanagioti, H.; Vinitnantharat, S.; Werner, D. Valorisation of Agricultural Waste Derived Biochars in Aquaculture to Remove Organic Micropollutants from Water—Experimental Study and Molecular Dynamics Simulations. *J. Environ. Manag.* **2021**, *300*, 113717. [CrossRef]

66. Rissouli, L.; Benicha, M.; Chabbi, M. Contribution to the Elimination of Linuron by the Adsorption Process Using Chitin and Chitosan Biopolymers. *J. Mater. Environ. Sci.* **2016**, *7*, 531–540.

67. Benaouda, B.; Iman, G.; Michalkiewicz, B. Study on Anionic Dye Toxicity Reduction from Simulated Media by MnO2/Agro-Biomass Based-AC Composite Adsorbent. *Ind. Crops Prod.* **2024**, *208*, 117789. [CrossRef]

68. Edet, U.A.; Ifelebuegu, A.O. Kinetics, Isotherms, and Thermodynamic Modeling of the Adsorption of Phosphates from Model Wastewater Using Recycled Brick Waste. *Processes* **2020**, *8*, 665. [CrossRef]

69. McCabe, W.C.; Smith, J.C.; Harriot, P. Unit Operations of Chemical Engineering. *Choice Rev. Online* **1993**, *30*, 30–6200. [CrossRef]

70. Mozaffari Majd, M.; Kordzadeh-Kermani, V.; Ghalandari, V.; Askari, A.; Sillanpää, M. Adsorption Isotherm Models: A Comprehensive and Systematic Review (2010−2020). *Sci. Total Environ.* **2022**, *812*, 151334. [CrossRef] [PubMed]

71. Sadasivam, S.; Krishna, S.K.; Ponnusamy, K.; Nagarajan, G.S.; Kang, T.W.; Venkatesalu, S.C. Equilibrium and Thermodynamic Studies on the Adsorption of an Organophosphorous Pesticide onto "Waste" Jute Fiber Carbon. *J. Chem. Eng. Data* **2010**, *55*, 5658–5662. [CrossRef]

72. Senthilkumaar, S.; Krishna, S.K.; Kalaamani, P.; Subburamaan, C.V.; Subramaniam, N.G. Adsorption of Organophosphorous Pesticide from Aqueous Solution Using "Waste" Jute Fiber Carbon. *Mod. Appl. Sci.* **2010**, *4*, 67. [CrossRef]

73. Shoushtarian, F.; Moghaddam, M.R.A.; Kowsari, E. Efficient Regeneration/Reuse of Graphene Oxide as a Nanoadsorbent for Removing Basic Red 46 from Aqueous Solutions. *J. Mol. Liq.* **2020**, *312*, 113386. [CrossRef]

74. Santo, D.E.; Dusman, E.; da Silva Gonzalez, R.; Romero, A.L.; dos Santos Gonçalves do Nascimento, G.C.; de Souza Moura, M.A.; Bressiani, P.A.; Filipi, Á.C.K.; Gomes, E.M.V.; Pokrywiecki, J.C.; et al. Prospecting Toxicity of Octocrylene in *Allium cepa* L. and *Eisenia fetida* Sav. *Environ. Sci. Pollut. Res.* **2023**, *30*, 8257–8268. [CrossRef] [PubMed]

75. Moura, M.A.S.; Nascimento, G.C.S.G.; Valarini, O.; Peron, A.P.; Souza, D.C. Application of Salvinia Biloba Raddi. in the Phytoextraction of the Emerging Pollutant Octocrylene in an Aquatic Environment. *Processes* **2024**, *12*, 1631. [CrossRef]

76. Todorovac, E.; Durmisevic, I.; Cajo, S.; Haverić, A.; Mesic, A. Evaluation of DNA and Cellular Damage Caused by Methyl-, Ethyl- and Butylparaben in Vitro. *Toxicol. Environ. Chem.* **2021**, *103*, 85–103. [CrossRef]